Verification of the WALE large eddy simulation model for adaptive lattice Boltzmann methods implemented in the AMROC framework

Christos Gkoudesnes and Ralf Deiterding

Abstract We detail the verification of the WALE large eddy simulation turbulence model for application in cell-based lattice Boltzmann methods, as implemented in our generic Cartesian structured adaptive mesh refinement framework AMROC. We demonstrate how to effectively apply the test case of decaying homogeneous isotropic turbulence to verify the core WALE implementation against higher resolved direct numerical simulations and the constant-coefficient Smagorinsky turbulence model. Both standard and regularised single relaxation collision models are analysed systematically. While our results confirm the established observation that the standard collision model yields less dissipative energy spectra, novel quantitative evidence is given that this positive behaviour comes at the cost of unphysical perturbations in high wavenumbers. In order to allow unaltered application of the finite-difference stencils intrinsic to the WALE approach in real-world flow situations, a new method is presented for ensuring consistent boundary conditions in microscopic distribution functions as well as in macroscopic variables. The benefit of the proposed technique is shown for dynamically adaptive simulations of flow around a sphere at Reynolds number 1000 and compared to a large eddy simulation using the constant-coefficient Smagorinsky model.

1 Introduction

In recent years the lattice Boltzmann method (LBM) [20, 32] has achieved stupendous success in a variety of scientific fields. Application examples can be found for

Christos Gkoudesnes
Aerodynamics and Flight Mechanics Research Group, School of Engineering, University of Southampton, SO16 7QF, United Kingdom e-mail: C.Gkoudesnes@soton.ac.uk

Ralf Deiterding
Aerodynamics and Flight Mechanics Research Group, School of Engineering, University of Southampton, SO16 7QF, United Kingdom e-mail: R.Deiterding@soton.ac.uk

instance in [1, 2, 16, 23, 30, 34, 35]. Its computationally inexpensive numerical scheme, straightforward parallelisation and close to linear parallel scalability make it a powerful alternative for subsonic flow simulations compared to the mainstream computational fluid dynamics solvers that discretise the Navier-Stokes equations and usually employ finite volume schemes. Thanks to a time-explicit numerical update and intrinsically low numerical dissipation, the LBM lends itself particularly to large eddy simulations (LES) of engineering applications involving high Reynolds number flows. The employment of Cartesian meshes, characteristic for the LBM, in addition allows easy and automatic mesh generation and hence has the potential of reducing the time for setting up a simulation considerably, particularly with complex geometries. However, the drawback of the Cartesian approach is that a significant number of cells usually needs to be deployed in the vicinity of the body in order to accurately approximate its shape. In the case of uniform grids, this can lead to prohibitively large meshes. A possibility to mitigate this issue is the extension of the LBM to body-fitted structured [29] or hybrid meshes [10]. The other – more common – approach is the use of levels of Cartesian refinement. This approach can be further optimised by the implementation of solution adaptive mesh refinement (AMR).

The AMROC (Adaptive Mesh Refinement in Object-oriented C ++) framework [7] implements patch-based, structured adaptive mesh refinement (SAMR) generically for time-explicit finite volume methods. The LBM has been incorporated into AMROC by formulating it on cell-based data structures; treatment of embedded boundaries with a level-set-based ghost-fluid-type approach allows for an effective handling of moving solid bodies. Examples of successful AMROC-LBM simulations, primarily in the laminar flow regime, can be found for instance in [8, 19, 12, 9, 11, 21]. The present paper reports on verification and validation of a variety of new developments in the AMROC-LBM solver, in particular the wall-adapting local eddy-viscosity (WALE) turbulence model [26] and the newly implemented regularised single relaxation time (SRT) collision operator [22]. In the procedure of applying LES models, that are based on finite difference stencils, a new algorithm for imposing macroscopic variables in ghost cells, after the application of "bounce-back" boundary conditions, is presented and tested here for the very first time. Two validation tests are discussed in detail, namely the decaying homogeneous isotropic turbulence in a periodic box benchmark and turbulent flow around a sphere at Reynolds number 1000. Comparing the spectra from the STAndard (STA) and REGularised (REG) SRT operators in the former case, useful information will be extracted. The efficiency and performance of the WALE model will also be cross-verified against the Constant SMAgorinsky (CSMA) model.

The paper is organised as follows: In Sec. 2 we present the LBM equations both for the STA and REG SRT operators, the formulas for the CSMA and WALE models, and the SAMR strategy as implemented in AMROC. Section 3 details the improved boundary condition implementation in AMROC-LBM, both for the domain and the embedded non-Cartesian surface boundaries, and the new algorithm for imposing microscopic as well as macroscopic variables in ghost cells will be reported. The

results of the two validation test cases and their discussion can be found in Sec. 4. Finally, the conclusions are drawn in Sec. 5.

2 Methodology

In this section, we review the lattice Boltzmann method and the newly implemented REG SRT collision model. Moreover, the formulas describing the two LES models, employed in this paper, are introduced. Finally, we summarise the SAMR strategy that is applied in the AMROC-LBM solver.

2.1 Lattice Boltzmann method

The discrete lattice Boltzmann equation, describing the evolution of the distribution functions f_α with the SRT collision model and without an external force, reads

$$\partial_t\ f_\alpha + \mathbf{e}_\alpha \cdot \nabla f_\alpha = \tau^{-1}(f_\alpha^{\mathrm{eq}} - f_\alpha), \tag{1}$$

where τ is the discrete relaxation time. We chose the standard discretisation in space and time based on a finite difference scheme and a two-step procedure. The first operation, that is applied during the time step update, is the streaming

$$\check{f}_\alpha(\mathbf{x} + \mathbf{e}_\alpha \Delta t, t) = f_\alpha(\mathbf{x}, t), \tag{2}$$

where $\check{f}_\alpha$ is the intermediate value of the distribution function between the two steps. The second operation is the collision. For the STA SRT model, it is defined as

$$f_\alpha(\mathbf{x}, t + \Delta t) = \check{f}_\alpha(\mathbf{x}, t) + \frac{\Delta t}{\tau}(f_\alpha^{\mathrm{eq}}(\mathbf{x}, t) - \check{f}_\alpha(\mathbf{x}, t)). \tag{3}$$

The discrete relaxation time τ in LBM is given as

$$\tau = \frac{\nu + \Delta t c_s^2/2}{c_s^2}, \tag{4}$$

where ν is the kinematic viscosity and c_s is the physical speed of sound of the fluid. The number of the lattice velocities $\mathbf{e}_\alpha$ depends on the employed LBM model. In the current research work, the D3Q19 model was used, with the 19 lattice directions defined as

$$\mathbf{e}_\alpha = \begin{cases} 0, & w_\alpha = \frac{12}{36}, \quad \alpha = 0, \\ (\pm 1, 0, 0)c, (0, \pm 1, 0)c, (0, 0, \pm 1)c, & w_\alpha = \frac{2}{36}, \quad \alpha = 1, \ldots, 6, \\ (\pm 1, \pm 1, 0)c, (\pm 1, 0, \pm 1)c, (0, \pm 1, \pm 1)c, & w_\alpha = \frac{1}{36}, \quad \alpha = 7, \ldots, 18. \end{cases} \tag{5}$$

The notation c is the ratio $\Delta x/\Delta t$. The Maxwellian equilibrium distribution function is truncated to second order, yielding

$$f_\alpha^{\mathrm{eq}}(\mathbf{x},t) = w_\alpha\ \rho\left[1+\frac{\mathbf{e}_\alpha\cdot\mathbf{u}}{c_s^2}+\frac{(\mathbf{e}_\alpha\cdot\mathbf{u})^2}{2c_s^4}-\frac{\mathbf{u}\cdot\mathbf{u}}{2c_s^2}\right], \tag{6}$$

with the user option in AMROC-LBM to increase the latter approximation to third order for slightly improved accuracy and stability. The macroscopic variables density ρ, velocity vector $\mathbf{u}$ and pressure p can be evaluated through the first two moments of the distribution functions f_α as

$$\rho(\mathbf{x},t) = \sum_\alpha f_\alpha(\mathbf{x},t), \tag{7a}$$

$$\rho(\mathbf{x},t)u_i(\mathbf{x},t) = \sum_\alpha e_{\alpha i} f_\alpha(\mathbf{x},t), \tag{7b}$$

$$p(\mathbf{x},t) = \rho(\mathbf{x},t)\ c_s^2. \tag{7c}$$

At this point, it is helpful to introduce the non-equilibrium part of the distribution functions, $f_\alpha^{\mathrm{neq}}(\mathbf{x},t) = f_\alpha(\mathbf{x},t) - f_\alpha^{\mathrm{eq}}(\mathbf{x},t)$, and, by utilisation of the second moment, to obtain the momentum flux tensor Π_{ij}^{neq} as

$$\Pi_{ij}^{\mathrm{neq}} = \sum_\alpha e_{\alpha i} e_{\alpha j} f_\alpha^{\mathrm{neq}}(\mathbf{x},t). \tag{8}$$

This tensor is analogous to the strain rate in the Navier-Stokes equations and will be useful for the subsequent discussion.

2.1.1 Regularised single relaxation time collision model

To further improve the stability of the AMROC-LBM solver for high Reynolds number flows, a second collision model, namely REG SRT, proposed by Latt and Chopard [22], has been recently implemented. The idea is to *regularise* the non-equilibrium part of the distribution functions before one applies the collision step. This procedure reads

$$f_\alpha^{(1)}(\mathbf{x},t) = \frac{w_\alpha}{2c_s^4} Q_{\alpha ij}\Pi_{ij}^{\mathrm{neq}}, \tag{9}$$

where $Q_{\alpha ij} = e_{\alpha i}e_{\alpha j} - c_s^2\delta_{ij}$ and Π_{ij}^{neq} is estimated from Eq. (8). In this way, the non-equilibrium part retains the symmetry that is imposed by its relation with the viscous stress tensor and the strain rate. This extra step transforms the computation of the collision operation, Eq. (3), to

$$f_\alpha^{\mathrm{reg}}(\mathbf{x},t+\Delta t) = f_\alpha^{\mathrm{eq}}(\mathbf{x},t) + (1-\frac{\Delta t}{\tau})\check{f}_\alpha^{(1)}(\mathbf{x},t). \tag{10}$$

2.2 Large eddy simulation

In AMROC-LBM the integration of the LES models in the solver is based on the eddy viscosity approach [17]. In the case of a direct numerical simulation (DNS) with the LBM, the discrete relaxation time Eq. (4) is a global variable depending only on the physical speed of sound, the viscosity of the gas and the time step. The idea is that altering the relaxation time is analogous to changing the mean free path of the particles. Invoking the mixing length theory of Prandtl, one can argue that altering the mean free path is equivalent to changing the viscosity, leading to the idea of a turbulent eddy viscosity ν_t. The general formula to calculate the eddy viscosity is

$$\nu_t = (C\Delta x)^2 OP_{\mathrm{LES}}, \tag{11}$$

where C is a constant and OP_{LES} is a time scale estimated differently by each LES model. Therefore, in the case of an LBM LES, the physical viscosity is replaced by an effective viscosity $\nu^\star = \nu + \nu_t$. This alteration also affects the calculation of the discrete relaxation time τ which is replaced by an effective value $\tau^\star$.

2.2.1 Constant Smagorinsky model

For the case of the CSMA model [31] the eddy viscosity is computed as

$$\nu_t = (C_S\Delta x)^2 |\overline{S}|, \tag{12}$$

where $|\overline{S}| = \sqrt{2\overline{S}_{ij}\overline{S}_{ij}}$ is the intensity of the filtered strain rate. The constant C_S is a user parameter, with a usual value between 0.1 and 0.2. As already mentioned in Section 2.1.1, the non-equilibrium part of the distribution function f_α^{neq} can be used to estimate the strain rate locally per cell as

$$\overline{S}_{ij} = -\frac{1}{2\rho c_s^2 \tau^\star}\overline{\Pi}_{ij}^{\mathrm{neq}}\,. \tag{13}$$

One can substitute Eq. (13) in Eq. (12) and after some algebra an explicit equation for the effective discrete relaxation time $\tau^\star$ in each cell is retrieved:

$$\tau^\star = \frac{\tau}{2} + \sqrt{\frac{\tau^2}{4} + \frac{C_S^2\Delta x^2|\overline{\Pi}_{ij}^{\mathrm{neq}}|}{2\rho c_s^4}}, \tag{14}$$

with τ computed by Eq. (4).

2.2.2 Wall-adapting local eddy-viscosity model

The idea of the WALE model is to employ a more advanced operator for the characteristic time scale OP_{LES} that can effectively reduce the eddy viscosity to zero at the wall, thereby reproducing the proper scaling $\nu_t \sim y^{+^3}$ without the need for a damping function or any other location-dependent strategy [26]. The new operator is a function both of the strain rate S_{ij} and the rotation rate Ω_{ij}. It reads

$$OP_{\mathrm{WALE}} = \frac{(\mathcal{J}_{ij}\mathcal{J}_{ij})^{\frac{3}{2}}}{(\overline{S}_{ij}\overline{S}_{ij})^{\frac{5}{2}} + (\mathcal{J}_{ij}\mathcal{J}_{ij})^{\frac{5}{4}}}, \tag{15}$$

where $\mathcal{J}_{ij}$ is

$$\mathcal{J}_{ij} = \overline{S}_{ik}\overline{S}_{kj} + \overline{\Omega}_{ik}\overline{\Omega}_{kj} - \frac{1}{3}\delta_{ij}(\overline{S}_{mn}\overline{S}_{mn} - \overline{\Omega}_{mn}\overline{\Omega}_{mn}). \tag{16}$$

Therefore, in this case the eddy viscosity is calculated as

$$\nu_t = (C_w \Delta x)^2 OP_{\mathrm{WALE}}, \tag{17}$$

where C_w is the constant of the model and is equal to 0.5.

Compared to the CSMA model, which retains the locality of the collision step, the WALE model is based on central finite differences for estimating the rotation and strain rates. This stencil operation destroys the locality of the WALE collision operation, adds extra computational burden and, as we will present below, requires special attention in the application of some boundary conditions.

2.3 Structured dynamic mesh adaptation

The AMROC framework provides the capability of dynamic mesh adaptation, utilising user-defined refinement indicators on fully parallelised meshes. Its AMR strategy is based on the block-structured and recursive adaptive mesh refinement method for hyperbolic conservation laws after Berger and Collela [3]. By formulating the LBM on cell-based data structures, the method can be made to fit smoothly into the SAMR execution procedure. A positive side effect of the cell-based formulation is that the scheme becomes conservative in ρ and $\rho\mathbf{u}$.

In the SAMR approach, finite volume cells are clustered with a special algorithm into non-overlapping rectangular grids. The grids have a suitable layer of halo cells for synchronization and applying inter-level and physical boundary conditions. Refinement levels are integrated recursively and by updating the sequence of grids on each level in a for-loop using the same numerical update routine. The spatial mesh width Δx_l and the time step Δt_l on level l are refined by the same factor r_l, where we assume $r_l \geq 2$ for $l > 0$ and $r_0 = 1$. In order to ensure that the same gas, with identical speed of sound and kinematic viscosity is approximated on all levels of

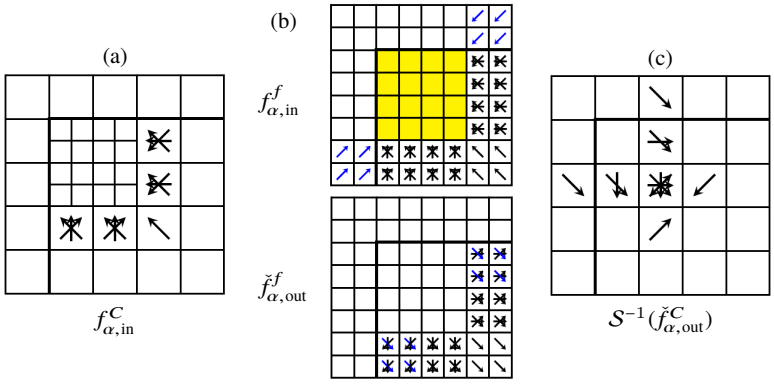

Fig. 1: Visualization of distributions involved in necessary data exchange at a coarse-fine boundary. The thick black lines indicate a physical boundary. (a) Coarse distributions going into fine grid; (b) ingoing interpolated fine distributions in halos (top), outgoing distributions in halos after two fine-level transport steps (bottom); (c) averaged distributions replacing coarse values before update is repeated in cells next to boundary.

the SAMR hierarchy, with the alteration of Δx_l and thus Δt_l, the discrete relaxation time τ cannot be a constant but needs to be adjusted according to Eq. (4) for the update on each level. In addition to this, the interface region requires a specialized treatment. Distinguishing between the streaming $\mathcal{S}$, Eq. (2), and collision C, Eq. (3), the crucial steps of our method are:

1. Use coarse grid distributions $f^C_{\alpha,\mathrm{in}}$ that propagate into the fine grid, cf. Fig. 1a, to construct initial fine grid halo values $f^f_{\alpha,\mathrm{in}}$ by interpolation (Fig. 1b, top).
2. Stream $\check{f}^f_\alpha := \mathcal{S}(f^f_\alpha)$ on entire fine mesh. Collision $f^f_\alpha := C(\check{f}^f_\alpha)$ is applied only in the interior cells (yellow in Fig. 1b, top). Repeat $r_l - 1$ times.
3. Average outgoing distributions from fine grid halos (Fig. 1b, bottom) to obtain $\check{f}^C_{\alpha,\mathrm{out}}$.
4. Reverse streaming for averaged outgoing distributions, $\bar{f}^C_{\alpha,\mathrm{out}} := \mathcal{S}^{-1}(\check{f}^C_{\alpha,\mathrm{out}})$, and overwrite those in the previous coarse grid time step, cf. Fig. 1c.
5. Repeat LBM update on coarse grid cells next to coarse-fine boundary only.

This algorithm is computationally equivalent to the method by Chen *et al.* [5] but tailored to the SAMR recursion that updates coarse grids in their entirety before fine grids are computed. Because of the nonlinearity of the collision operator C it becomes necessary under this paradigm to repeat the LBM update for those coarse grid cells that share a face or corner with a fine grid. A comprehensive verification of the adaptive method in AMROC-LBM can be found in [12].

3 Boundary conditions in AMROC-LBM

The utilisation of halo or ghost cells is intrinsic to the SAMR approach. In order to achieve an efficient and parallel update of the subgrids on each level of the hierarchy, it is of crucial importance to synchronise and apply boundary conditions in ghost cells before the execution of the numerical update routine. Similarly, the modification of internal cells in order to realise geometrically complex embedded wall boundary conditions is in AMROC-LBM equally carried out immediately before the LBM update. While the routines for synchronisation and first-order-accurate inter-level boundary conditions in AMROC are generic, cf. [7], special attention is necessary to implement high-quality physical boundary conditions for the LBM.

3.1 Domain boundaries

Two types of domain boundaries are used in the current paper. Both are based on the idea of [36] and are similar to the strategy applied in [33] for domain boundaries. The basic idea is the reconstruction of the distribution functions in the ghost cells through the extrapolation of the macroscopic variables and the non-equilibrium part from the neighbouring interior cell in the normal direction.

3.1.1 Inlet

In the case of an inlet boundary, the vector of velocities is imposed and the density $\rho(\mathbf{x}_{\mathrm{BC}})$ in the boundary ghost cell is unknown. Assuming a zero gradient, the density of the first neighbouring normal interior fluid cell $\rho(\mathbf{x}_{\mathrm{F}})$ is extrapolated as

$$\rho(\mathbf{x}_{\mathrm{BC}}) = \rho(\mathbf{x}_{\mathrm{F}}). \tag{18}$$

Having obtained the density, one can proceed with estimating the equilibrium part $f_\alpha^{\mathrm{eq}}(\mathbf{x}_{\mathrm{BC}})$ of the distribution function by applying Eq. (6). The same extrapolation can be used to estimate a value for the non-equilibrium part as

$$f_\alpha^{\mathrm{neq}}(\mathbf{x}_{\mathrm{BC}}) = f_\alpha(\mathbf{x}_{\mathrm{F}}) - f_\alpha^{\mathrm{eq}}(\mathbf{x}_{\mathrm{F}}). \tag{19}$$

With these two values one can now reconstruct the distribution function in the boundary ghost cell as

$$f_\alpha(\mathbf{x}_{\mathrm{BC}}) = f_\alpha^{\mathrm{eq}}(\mathbf{x}_{\mathrm{BC}}) + f_\alpha^{\mathrm{neq}}(\mathbf{x}_{\mathrm{BC}}). \tag{20}$$

3.1.2 Outlet

In the case of the outlet boundary, the density $\rho(\mathbf{x}_{\mathrm{BC}})$ is imposed and the velocity field needs to be extrapolated from the normal neighbouring interior fluid cell. Following the same methodology as in case of the inlet boundary, the extrapolation formula is

$$\mathbf{u}(\mathbf{x}_{\mathrm{BC}}) = \mathbf{u}(\mathbf{x}_{\mathrm{F}}). \tag{21}$$

Having obtained both density and velocity in the ghost cell location, the equilibrium functions, Eq. (6), can be calculated. The non-equilibrium part is also extrapolated following Eq. (19). Finally, the reconstruction of $f_\alpha(\mathbf{x}_{\mathrm{BC}})$ is according to Eq. (20).

3.2 Embedded wall boundaries

In the AMROC software, non-Cartesian boundaries are represented implicitly on the adaptive Cartesian grid by utilising a scalar level set function φ that stores the distance to the boundary surface. The boundary surface is located exactly at $\varphi = 0$ and the boundary outer normal in every mesh point can be evaluated as $\mathbf{n} = -\nabla\varphi/|\nabla\varphi|$ [6]. A fluid cell is treated as an embedded ghost cell if its midpoint satisfies $\varphi < 0$.

Real-world geometries are considered in AMROC as triangular surface meshes, cf. [7]. The computation of the level set distance information in every Cartesian cell midpoint could principally be accomplished by simply iterating over the entire surface mesh; yet, this would lead to detrimental performance for increasing problem size. Instead, we employ a specially developed algorithm based on characteristic reconstruction and scan conversion by Mauch [24] that is used to compute the distance exactly only in a small band around the embedded structure.

For imposing no-slip wall boundaries on the LBM, we choose in this paper the bounce-back algorithm of [4]. The idea of this methodology is to enhance the standard half-way bounce-back scheme with a spatial interpolation of first- or second-order accuracy to handle curved boundaries. The interpolation weight q is the ratio between the distance to the wall from the first fluid cell to the grid spacing. Based on the value of q and in case of the first-order-accurate interpolation, there are two possibilities:

$$f_{\mathrm{opp}(\alpha)}(\mathbf{x}_{\mathrm{BC}}) = 2q f_\alpha(\mathbf{x}_{\mathrm{F1}}) + (1-2q) f_\alpha(\mathbf{x}_{\mathrm{F2}}), \qquad q < 0.5, \tag{22a}$$

$$f_{\mathrm{opp}(\alpha)}(\mathbf{x}_{\mathrm{BC}}) = \frac{1}{2q} f_\alpha(\mathbf{x}_{\mathrm{F1}}) + \frac{(2q-1)}{2q} f_{\mathrm{opp}(\alpha)}(\mathbf{x}_{\mathrm{F1}}), \qquad q \geq 0.5. \tag{22b}$$

In the above equations, $\mathrm{opp}(\alpha)$ is the lattice direction opposite to α, $f_\alpha(\mathbf{x}_{\mathrm{F1}})$ is the distribution function located in the first neighbour cell in the lattice direction α, while $f_\alpha(\mathbf{x}_{\mathrm{F2}})$ is located in the second neighbour fluid cell in the same direction.

The difference between our implementation and the original approach is that the estimated distribution function is originally imposed at $f_{\mathrm{opp}(\alpha)}(\mathbf{x}_{\mathrm{F1}}, t + \Delta t)$, in

contrast to our case, which applies it to $f_{\mathrm{opp}(\alpha)}(\mathbf{x}_{\mathrm{BC}}, t)$. The subsequent streaming operation of the time step will transport it to the right fluid cell before the collision.

3.3 Imposing macroscopic variables in ghost cells

For the WALE model, central finite differences of the velocity field are needed to estimate the strain and rotation rates. In the case of the described in- and outlet boundary conditions, applying Eq. (7) yields suitable macroscopic variables in the ghost cells. However, a bounce-back boundary condition, such as in Sec. 3.2, imposes only some of the distribution functions. Directly applying Eq. (7) would create questionable moment values that could dramatically affect the estimation of the eddy viscosity in the vicinity of the wall, resulting in inaccurate results.

To deal with this issue, we propose a new algorithm that is employed after the boundary condition and allows imposing the macroscopic variables without affecting the distribution functions that will be streamed to fluid cells and have been imposed by the boundary conditions in microscopic distribution functions. The idea is to alter the rest, i.e., the outward streaming distribution functions such that the evaluation of Eq. (7) will yield reasonable values. During this procedure, the algorithm checks the lattice directions in order to decide which of them point to interior fluid cells and are needed to impose the microscopic boundary conditions. These directions, denoted as i, are marked as *non-free*. Simultaneously, one can estimate *partial* density and velocity field as

$$\delta\rho = \sum_i f_i, \quad i \in \textit{non-free directions}, \tag{23a}$$

$$\delta\rho\mathbf{u} = \sum_i \mathbf{e}_i f_i, \quad i \in \textit{non-free directions}. \tag{23b}$$

We index the group of the *free* directions with j. Assuming the groups of non-free and free directions have I and J elements, respectively, we have $n = I + J$, with $n = 19$ for instance for the D3Q19 model. The idea is to use the free directions to impose the four macroscopic variables, namely density ρ_0 and the three velocity components $\mathbf{u}_0$. In order for this algorithm to be functional, one needs to ensure that $J \geq 4$ for the ghost cell in question. Moreover, in order for the three components of the velocity to be specified, it must be ensured that for $\sum_j \mathbf{e}_j = (\alpha_1, \alpha_2, \alpha_3)$ the relations $\alpha_1, \alpha_2, \alpha_3 > 0$ hold true. In most scenarios, these two restrictions are satisfied and we also have $J > 4$, which results in the over-determined system

$$\rho_0 - \delta\rho = \sum_j f_j, \quad j \in \textit{free directions}, \tag{24a}$$

$$\rho_0\mathbf{u}_0 - \delta\rho\mathbf{u} = \sum_j \mathbf{e}_j f_j, \quad j \in \textit{free directions}. \tag{24b}$$

An efficient way to resolve this issue is the use of the equilibrium function Eq. (6) estimated by the imposed macroscopic quantities, ρ_0 and $\mathbf{u}_0$. In this way, we can reduce the number of unknowns to four. At this point, we ignore the distribution function of the zero lattice direction f_0, which will be used to satisfy the density ρ_0. The next step is to loop over the rest of the *free* directions, starting from the direction with the smaller α, and impose the equilibrium values until we have only three unknown distributions. We index the group of K equilibrium distributions by k, and obviously $n = I + K + 4$. In this way we end up with a system of four equations with four unknowns.

Initially, we have to solve the linear system of the three equations, indexed m, originating from the first moment:

$$\rho_0 \mathbf{u}_0 - \delta\rho\mathbf{u} - \sum_k \mathbf{e}_k f_k^{\mathrm{eq}} = \sum_m \mathbf{e}_m f_m \implies \mathbf{b} = \mathbf{A}\mathbf{f}. \tag{25}$$

In the current implementation, an LU-decomposition is employed to solve the above linear system. The last step is the evaluation of f_0 as

$$\rho_0 - \delta\rho - \sum_k f_k^{\mathrm{eq}} - \sum_m f_m = f_0. \tag{26}$$

It is important to mention that the ascending order during the step of the equilibrium functions is vital for the stability of the algorithm. In case that at least one of the members of the m group belongs to $\alpha \in [1, 6]$, the matrix $\mathbf{A}$ will be singular resulting in no available solution for the system of Eq. (25).

The proposed algorithm can also be applied straightforwardly to the D3Q27 stencil and can also be used in 2D with the D2Q9 stencil. As for the imposed velocity $\mathbf{u}_0$, as a first attempt and following a ghost-fluid approach, we use in this paper the interpolated velocity at the point $\mathbf{x}_{\mathrm{BC}} + 2\varphi\mathbf{n}$. However, one could increase the accuracy, particularly in a turbulent boundary layer, by assuming the law of the wall in the normal direction and thus estimating the velocity components.

4 Results

To illustrate the capabilities of the new implementations in the AMROC-LBM solver, we present two benchmark cases, namely decaying homogeneous isotropic turbulence in a periodic box and the flow around a sphere at Reynolds number $\mathrm{Re} = 1000$. The first test case serves the purpose of verifying the core LES models and investigating their interplay with the two available collision operators. The second test, on the other hand, verifies their integration with various boundary conditions, particularly embedded complex walls, and the AMR algorithm. Moreover, the proposed algorithm for imposing macroscopic variables in ghost cells will also be tested and evaluated.

4.1 Decaying homogeneous isotropic turbulence

The numerical domain for the decaying homogeneous isotropic turbulence test case is a cube with side length $L = 2\pi$. Periodic boundary conditions are applied at all sides. Assuming a uniform grid, this setup provides a unique and convenient way to test LES models without disturbances arising from physical boundary conditions or the resolution interfaces between levels of AMR.

Our initialisation of the flow field is based on the final saved iteration of a forced homogeneous isotropic turbulence case presented previously in [13, 14]. In this scenario, we restart the simulation in the AMROC-LBM solver but deactivate the force. Suitable local volume averaging is applied when creating the initial solutions for the lower resolutions. To ensure a fair comparison, all simulations in this chapter have been initialised based on a DNS with a resolution of 512^3 running with the REG SRT collision model. The reason for this choice is that the force has created slightly different Reynolds number flows for the case of STA and REG SRT and thus a direct comparison of the curves would be difficult. The initial Reynolds number based on the integral length scale λ is 80. Moreover, a field arising from the regularised model can safely be assumed to be more accurate, and it can be expected that the effect of the initial solution will fade away over time. We have also restarted the STA SRT simulations from the non-regularised DNS of 512^3, and the results were found to be identical to the ones presented below.

In the plots in this chapter, we will compare two resolutions, namely 128^3 and 32^3 cells, for two turbulence models currently available in the AMROC-LBM solver. The first one is the WALE, which we want to verify and evaluate, and the second is the CSMA with $C_S = 0.1$. Simultaneously, we will compare the two aforementioned collision models, STA and REG SRT. Additionally, a DNS with the REG SRT collision model with 512^3 cells will be shown as a reference solution. All simulations have run for a final time of 1000 time units.

Figure 2 presents the evolution of the turbulent kinetic energy k and dissipation rate ε for the resolution of 128^3 cells normalised by the initial data of the DNS of 512^3. The collapse of the LES curves with the reference DNS for the whole time in the case of the kinetic energy and for most of the time for the dissipation rate is imminent. The discrepancies appearing in the initial part for the dissipation rate are the effect of the local volume averaging resulting in fewer small eddies and thus a smaller initial value for ε. Therefore, examining these two plots, we cannot identify any differences between the two LES and the two collision models.

From the theory of decaying homogeneous isotropic turbulence, we expect that power-laws of the type $k \sim (t + t_0)^{-n}$ and $\varepsilon \sim (t + t_0)^{-n-1}$ can describe the slopes in the current plots. In Fig. 2, we have also estimated the exponent $n = 1.4$, a value in the expected range in agreement with literature [18].

Instantaneous 3D energy spectra and pressure fluctuation spectra at $t = 98.17$ time units are given in Fig. 3. Examining the energy spectra, their collapse in the energy-containing range is a strong proof that the LES models do not affect the large eddies, which is anticipated. Moreover, CSMA with $C_S = 0.1$ and WALE have produced identical results in the case of the same collision model, providing

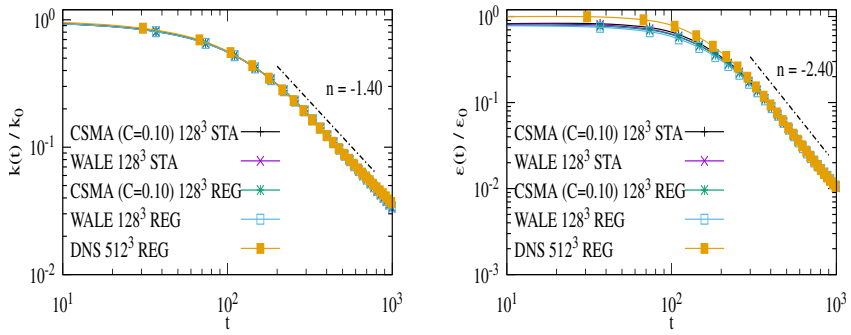

Fig. 2: Evolution of the turbulent kinetic energy k (left) and dissipation rate ε (right) for CSMA with $C_S = 0.1$ and WALE at a resolution of 128^3 cells for both STA and REG SRT. The DNS of 512^3 resolution with REG SRT has been added as a reference.

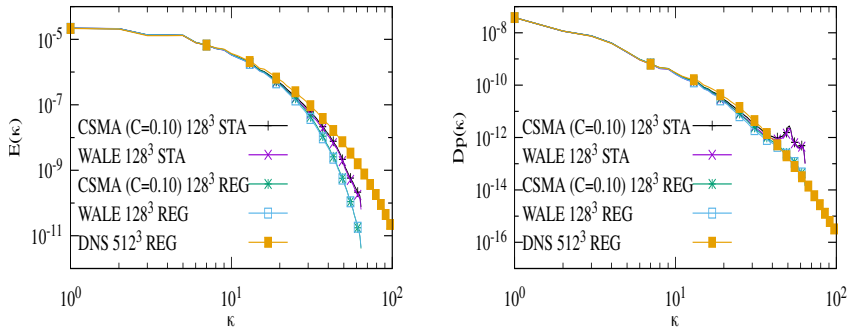

Fig. 3: Instantaneous energy spectra (left) and pressure fluctuation spectra (right) of the CSMA with $C_S = 0.1$ and the WALE for both STA and REG SRT for the resolution of 128^3 cells at $t = 98.17$ time units. The curves of the REG DNS on 512^3 cells are shown as a reference.

first evidence for the correctness of the WALE implementation. However, STA SRT seems to produce less dissipative results in the high wavenumber region, as it returns values closer to the DNS reference solution. This observation has also been recently reported by Nathen *et al.* [25].

Inspecting the pressure fluctuation spectra, one can notice that using the STA collision model the amount of small eddies has been considerably increased. It turns out that the departure of the energy spectra in the dissipation range for the two collision models coincides with this increase. Hence, we can speculate that the less dissipative behaviour of the STA SRT model is not because the small eddies carry more energy but because of an artificial rise in their numbers. Contrarily, the REG SRT model has estimated a solution much closer to the reference. We explain this

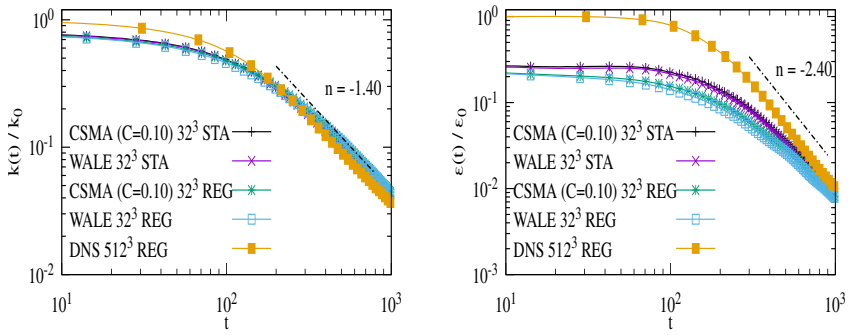

Fig. 4: Evolution of the turbulent kinetic energy k (left) and dissipation rate ε (right) for CSMA with $C_S = 0.1$ and WALE at a resolution of 32^3 cells for both STA and REG SRT. The DNS of 512^3 with REG SRT has been added as a reference.

observation with the fact that the regularisation procedure is constructed to impose the symmetries of the strain rate S_{ij} in the non-equilibrium part of the distribution function, Eq. (13), while reliably maintaining $\sum \mathbf{e} f^{\text{neq}} = \sum f^{\text{neq}} = 0$. The latter is not always guaranteed in the case of the STA SRT model [22], which can result in conservation errors in density and momentum, i.e., non-physical behaviour in the collision step. Such errors occur in particular for high Reynolds numbers or Mach numbers close to the LBM stability threshold.

To challenge the models more, Fig. 4 shows the evolution of k and ε for the case of the resolution of 32^3 cells. No combination of models is able to capture the reference curve of the kinetic energy in the initial phase exactly, although there are no evident discrepancies among them. The deviation from the DNS result is even larger for the dissipation rate, where only in the last time units there is a convergence of all the curves. The most interesting feature of this plot is the deviation of the curves of the STA and REG counterparts in the initial part of the simulation, with the former to show an observably less dissipative behaviour.

Following the same procedure, Fig. 5 presents the instantaneous 3D energy and pressure fluctuation spectra at $t = 98.17$. Due to the extreme coarsening of the grid, the energy of the big eddies has been slightly overestimated by both LES and collision models. Again, the STA SRT operator has returned a less dissipative spectra in high wavenumbers. On the other hand, examining the pressure fluctuation spectra, the STA SRT model overestimates the small scales compared to the REG SRT model and the DNS. However, it is capable of following the DNS trend for more wavenumbers in contrast to the REG SRT that underpredicts the reference solution in the small scales.

Another important observation from the pressure fluctuation plot is the deviation of the WALE STA and CSMA STA models from the DNS in high wavenumbers. This deviation does not appear for the case of the REG collision model where the curves are identical. As mentioned previously, the CSMA estimates the strain rate locally

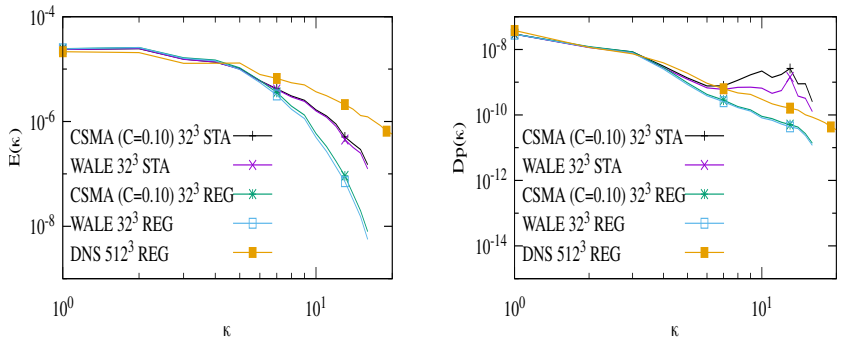

Fig. 5: Instantaneous energy spectra (left) and pressure fluctuation spectra (right) of the CSMA with $C_S = 0.1$ and the WALE for both STA and REG SRT for the resolution of 32^3 cells at $t = 98.17$. The curves of the REG DNS on 512^3 cells are shown as a reference.

based on the non-equilibrium part of the distribution function while WALE applies finite differences. By reducing the resolution and thus increasing Δx and Δt, we have reduced the value of τ. This reduction leads to a higher value for the factor $\Delta t/\tau$ in the collision step, amplifying any inaccuracies arising from the imprecise evaluation of the non-equilibrium part in the case of the STA SRT operator. The estimation of the first-order moments, and thus the velocity components, is expected to be more accurate than the second-order moments, leading to an improved prediction of the strain rate based on a finite-difference stencil.

Finally, Fig. 6 shows the instantaneous vorticity contours at $t = 98.17$ time units of the aforementioned models for the case of 128^3 cells. All combinations of models are able to capture the majority of the large eddies appearing in the reference solution of the DNS. Comparing the LES models, there are no apparent discrepancies, although the CSMA has produced slightly more small eddies. On the other hand, it is evident that the STA SRT model has predicted more small scales compared to the REG SRT, confirming our previous expectation from the pressure fluctuation plots.

4.2 Sphere at Reynolds number 1000

To verify the coupling of the LES models with domain and embedded solid boundaries, and also with the AMR algorithm, the benchmark of flow around a sphere of diameter D at Reynolds number 1000 is selected. A computational domain of dimensions $[-2D, 6D] \times [-2D, 2D] \times [-2D, 2D]$ is used. The domain boundary conditions from Sec. 3.1 are applied, where an inlet boundary condition is imposed on the left side and outlet boundary conditions are applied at all other sides. The no-slip wall boundary condition on the body is modelled with the Bouzidi bounce-back condition, as sketched in Sec. 3.2. The mesh adaptation was set up to run with five levels

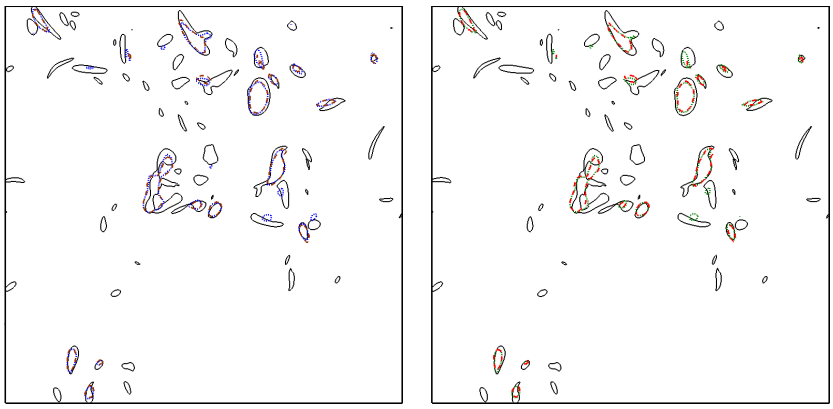

Fig. 6: Contours of vorticity magnitude ($|\omega| = 0.25$) at $t = 98.17$ time units, for the CSMA with $C_S = 0.1$ (left) STA (blue dotted) and REG (brown dashed) and for the WALE (right) STA (green dotted) and REG (red dashed) at a resolution of 128^3 cells. The black solid line is the DNS with a resolution of 512^3 given as a reference.

in total with a refinement factor $r_l = 2$ for all levels. The mesh width of the coarsest grid is $\Delta x = D/20$. The scaled gradient [7] of the vorticity magnitude was chosen as refinement indicator with a threshold value of 100. For the WALE model, we have also employed and tested the new algorithm for imposing macroscopic variables in ghost cells discussed in Sec. 3.3. The flow field has been initialised with the inlet velocity and an initial value for density.

Two simulations are discussed; one using the CSMA model with $C_S = 0.12$ and the other using the WALE model. Both computations use the REG SRT collision model. This decision was based on the superior behaviour of the REG SRT operator in the previous test case. The left plot of Fig. 7 visualises by colour the velocity magnitude for the case of CSMA in two planes and on an isosurface of vorticity magnitude for the value 100 at a time when the wake has been established. The shading in the right plot presents the distribution of the numerical domain to the employed processors and in addition the automatically refined mesh at the same time. It is evident that the refinement follows the isosurface closely. Figure 8 displays the two corresponding plots for the case of the WALE model. Comparing the results of the two turbulence models, there are no significant discrepancies, and both computations exhibit a very similar 3D wake structure and according mesh refinement. Minor differences in both figures are due to the different nature of the two turbulence models. The CSMA tends to predict a more diffusive eddy viscosity field with higher values in the whole domain. This behaviour will invariably reduce the accuracy of the solution, but simultaneously has the positive effect of stabilising numerical fluctuations, e.g., from boundary conditions. On the other hand, WALE tends to estimate lower eddy viscosity values in the majority of the domain but predicts larger values in and around fluid features. This distinction is the reason for any difference in the wakes and hence the dynamically adapted meshes.

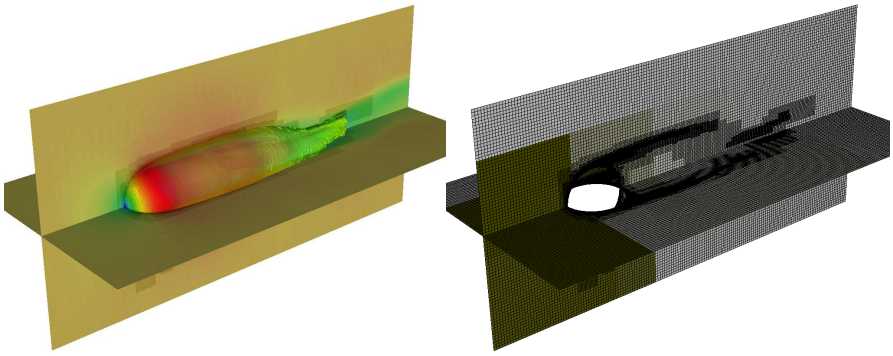

Fig. 7: Flow around a sphere at $\mathrm{Re} = 1000$ simulated with CSMA with $C_S = 0.12$. Left: Isosurface of vorticity and planes coloured by velocity magnitude. Right: Computational mesh and distribution to processors, indicated by shading.

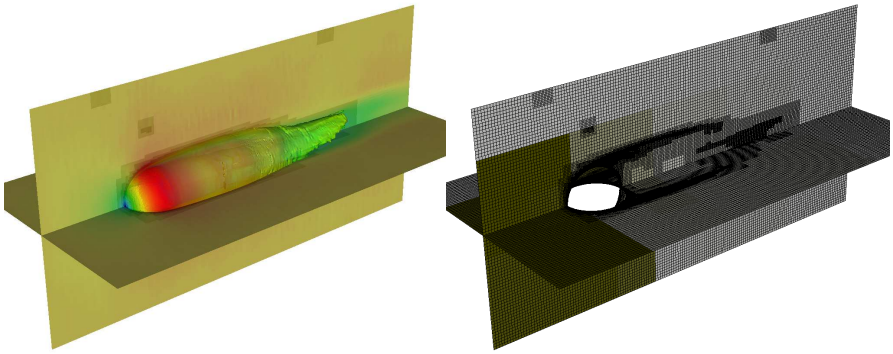

Fig. 8: Flow around a sphere at $\mathrm{Re} = 1000$ simulated with WALE. Left: Isosurface of vorticity and planes coloured by velocity magnitude. Right: Computational mesh and distribution to processors, indicated by shading.

To further enhance the comparison, Fig. 9 shows the vorticity magnitude for the two LES models in the xz-plane in logarithmic scale. Again, there are no significant differences between the shape and the shading for the two models. Examining the wake, particularly far away from the body, one can see some minor perturbations being emanated from the outlet boundary. The situation is slightly better for the CSMA model. Finally, Fig. 10 shows the evolution of the drag coefficients obtained during the last phase of the simulation for the two models. Both computations predict an average value of 0.461, which perfectly matches the theoretical value of 0.46 calculated from the standard drag curve for a sphere, and the value 0.464

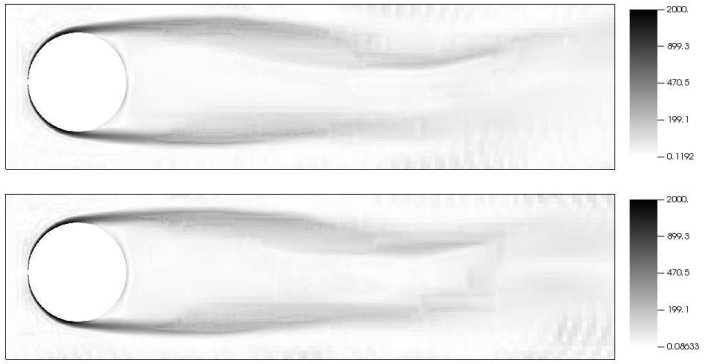

Fig. 9: Comparison of the vorticity magnitude between CSMA (top) and WALE model (bottom).

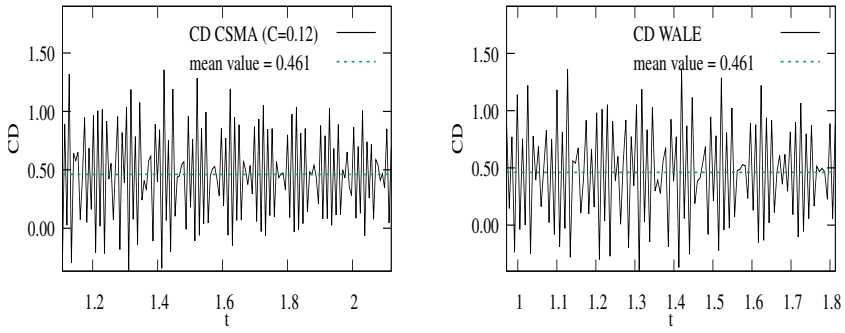

Fig. 10: Evolution of the drag coefficient CD for the CSMA model with $C_S = 0.12$ (left) and the WALE model (right). The dashed lines show the averaged values.

estimated with a recently proposed formula [15]. The predicted value also matches the one reported in [28] and is very close to the value of 0.48 reported in [27].

At this point, we evaluate the algorithm for imposing macroscopic variables in ghost cells from Sec. 3.3. To do so, we have also run the simulation of WALE without invoking the new treatment. Figure 11 presents the enlarged normalised eddy viscosity fields, at the same time step, for the WALE simulations with and without the use of the new algorithm. The normalisation of the eddy viscosity is based on the value of the physical viscosity. Examining the magnitude, it is clear that the LES model was not triggered considerably in the vicinity of the wall. There are two reasons for this: First, the WALE model is constructed to reduce the production of eddy viscosity close to the wall to represent the law of the wall more accurately. Secondly, in this specific case, the wall-near resolution is very high in order to approximate the curved geometry well and thus obtaining a very accurate estimation of the drag coefficient. The results confirm the consistency of the model in the case

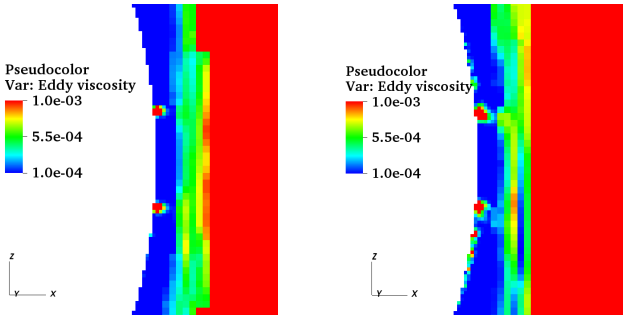

Fig. 11: Comparison of the enlarged normalised eddy viscosity at the back of the sphere with imposed macroscopic variables in ghost cells (left) and without (right).

of a high-resolution mesh for a wall-resolved LES. Comparing the two graphics, one can conclude that the use of the algorithm from Sec. 3.3 has reduced the formation of a band of large eddy viscosity values close to the wall.

We close this section with a discussion of the performance of the AMROC-LBM solver for the sphere test case. Both simulations ran for $120\,\mathrm{h}$ wall time using 64 cores of 2.6-GHz Intel Sandybridge processors. The initial size of the adaptive mesh for both cases is $\sim 8.7\,\mathrm{M}$ cells, while the final size is between 16 and $17\,\mathrm{M}$ cells. Application of the finest level with $\sim 5.3\,\mathrm{M}$ cells is restricted to the vicinity of the body. On average, the CSMA simulation required $27.65\,\mathrm{s}$ per iteration, while the WALE simulation took $32.26\,\mathrm{s}$, which corresponds to an added expense of only 17%. However, the final size of the mesh for the WALE simulation is also slightly larger than in the CSMA case, which altogether confirms that incorporating the more sophisticated WALE model into AMROC-LBM has resulted only in a moderate increase in computational time.

5 Conclusions

The main aim of this paper was to present the verification procedure of the WALE turbulence model recently implemented in our dynamically adaptive in-house lattice Boltzmann solver AMROC-LBM. The first step was simulating the test case of decaying homogeneous isotropic turbulence and comparing the energy and pressure fluctuation spectra with DNS of higher resolution and CSMA LES of the same resolution. Identical behaviour with the CSMA was confirmed, which – given the isotropy of this test case – verifies the algorithmic implementation of the core WALE model. The second step was to simulate the flow around a sphere at Reynolds number 1000 for both WALE and CSMA. There were no significant discrepancies between the two models in the case of the vorticity field, verifying the interplay of the new WALE implementation with boundary conditions and the AMR algorithm. The

drag coefficients from both LES were confirmed to be in excellent agreement with literature. In this specific case, the adaptive computation using the WALE model was found to be only 17% more expensive than with CSMA, which demonstrates that the increase in computational costs, when using the considerably more complex WALE model, can be kept modest.

For the simulation of the decaying homogeneous isotropic turbulence case, both the standard and regularised collision models have been used. In agreement with recent research studies, we have found that the energy spectra of the STA model are less dissipative. To further enhance the comparison, we have also presented pressure fluctuation spectra, which highlight the fact that the STA collision model produces a large amount of small-scale perturbations, not present in the REG results. This behaviour of the STA collision model is unphysical and likely intrinsic to the model's handling of the non-equilibrium part of the distribution function. Moreover, in the case of the lowest resolution and STA collision model, we have shown that the CSMA model, which estimates the strain rate locally based on the non-equilibrium part, tends to enhance these instabilities compared to the WALE model, which uses finite-difference stencils of macroscopic variables.

Finally, a new LBM boundary condition construction algorithm for imposing macroscopic variables in addition to inward-directed microscopic distributions has been proposed. For instance, in the case of bounce-back wall boundary conditions, the resulting macroscopic moments are not well defined. By imposing suitable values, the finite difference stencils can still be applied unaltered, hence yielding a plausible estimate for the eddy viscosity in the vicinity of the wall or other domain boundaries. A detailed analysis of the eddy viscosity from the WALE model close to the embedded wall, with and without the new algorithm, has confirmed the increased accuracy of our approach.

Acknowledgements This work was supported by UK Research and Innovation under the grant EP/N509747/1 with project number 1831845. The authors also acknowledge the use of the IRIDIS High-Performance Computing Facility and associated support services at the University of Southampton.

References

1. Aidun, C.K., Clausen, J.R.: Lattice-Boltzmann method for complex flows. Annu. Rev. Fluid Mech. **42**(1), 439–472 (2010)
2. Van den Akker, H.E.: Lattice Boltzmann simulations for multi-scale chemical engineering. Current Opinion in Chemical Engineering **21**, 67–75 (2018)
3. Berger, M., Colella, P.: Local adaptive mesh refinement for shock hydrodynamics. J. Comput. Phys. **82**, 64–84 (1988)
4. Bouzidi, M., Firdaouss, M., Lallemand, P.: Momentum transfer of a Boltzmann-lattice fluid with boundaries. Physics of Fluids **13**(11), 3452–3459 (2001)
5. Chen, H., Filippova, O., Hoch, J., Molvig, K., Shock, R., Teixeira, C., Zhang, R.: Grid refinement in lattice Boltzmann methods based on volumetric formulation. Physica A **362**, 158–167 (2006)

6. Deiterding, R.: A parallel adaptive method for simulating shock-induced combustion with detailed chemical kinetics in complex domains. Computers & Structures **87**, 769–783 (2009)
7. Deiterding, R.: Block-structured adaptive mesh refinement - theory, implementation and application. European Series in Applied and Industrial Mathematics: Proceedings **34**, 97–150 (2011)
8. Deiterding, R., Wood, S.L.: An adaptive lattice Boltzmann method for predicting wake fields behind wind turbines. In: A. Dillmann, G. Heller, E. Krämer, C. Wagner, C. Breitsamter (eds.) New Results in Numerical and Experimental Fluid Mechanics X, *Notes on Numerical Fluid Mechanics and Multidisciplinary Design*, vol. 132, pp. 845–857. Springer (2016)
9. Deiterding, R., Wood, S.L.: Predictive wind turbine simulation with an adaptive lattice Boltzmann method for moving boundaries. J. Phys. Conf. Series **753**, 082005 (2016)
10. Di Ilio, G., Chiappini, D., Ubertini, S., Bella, G., Succi, S.: Fluid flow around NACA 0012 airfoil at low-Reynolds numbers with hybrid lattice Boltzmann method. Computers & Fluids **166**, 200–208 (2018)
11. Feaster, J., Battaglia, F., Deiterding, R., Bayandor, J.: Validation of an adaptive meshing implementation of the lattice Boltzmann method for insect flight. In: Proc. of the ASME 2016 Fluids Engineering Division Summer Meeting, pp. FEDSM2016–7782, V01AT12A007. ASME (2016)
12. Feldhusen, K., Deiterding, R., Wagner, C.: A dynamically adaptive lattice Boltzmann method for thermal convection problems. J. Applied Math. and Computer Science **26**, 735–747 (2016)
13. Gkoudesnes, C., Deiterding, R.: Evaluating the lattice boltzmann method for large eddy simulation with dynamic sub-grid scale models. In: 11th Int. Symp. on Turbulence and Shear Flow Phenomena (2019)
14. Gkoudesnes, C., Deiterding, R.: Verification and validation of a lattice boltzmann method coupled with complex sub-grid scale turbulence models. In: VI International Conference on Particle-based Methods - Fundamentals and Applications (2019)
15. Goossens, W.R.: Review of the empirical correlations for the drag coefficient of rigid spheres. Powder Technology **352**, 350–359 (2019)
16. He, Y.L., Liu, Q., Li, Q., Tao, W.Q.: Lattice Boltzmann methods for single-phase and solid-liquid phase-change heat transfer in porous media: A review. International Journal of Heat and Mass Transfer **129**, 160–197 (2019)
17. Hou, S., Sterling, J., Chen, S., Doolen, G.D.: A lattice Boltzmann subgrid model for high Reynolds number flows. In: A.T. Lawniczak, R. Kapral (eds.) Pattern formation and lattice gas automata, vol. 6, pp. 151–166. Fields Inst Comm (1996)
18. Huang, M., Leonard, A.: Power-law decay of homogeneous turbulence at low Reynolds numbers. Physics of Fluids **6**(11), 3765–3775 (1994)
19. Kin, N., Deiterding, R., Wagner, C.: High-resolution simulation of side flow past a generic model of a high-speed train. In: A. Dillmann, G. Heller, E. Krämer, C. Wagner, C. Breitsamter (eds.) New Results in Numerical and Experimental Fluid Mechanics X, *Notes on Numerical Fluid Mechanics and Multidisciplinary Design*, vol. 132, pp. 421–431. Springer (2016)
20. Krüger, T., Kusumaatmaja, H., Kuzmin, A., Shardt, O., Silva, G., Viggen, E.M.: The lattice Boltzmann method: principles and practice. Springer Berlin Heidelberg, New York, NY (2016)
21. Laloglu, C., Deiterding, R.: Simulation of the flow around an oscillating cylinder with adaptive lattice Boltzmann methods. In: B.H.V. Ivanyi P. Topping, G. Varady (eds.) Proc. 5th Int. Conf. on Parallel, Distributed, Grid and Cloud Computing for Engineering. Civil-Comp Press (2017)
22. Latt, J., Chopard, B.: Lattice Boltzmann method with regularized pre-collision distribution functions. Mathematics and Computers in Simulation **72**(2-6), 165–168 (2006)
23. Li, Q., Luo, K., Kang, Q., He, Y., Chen, Q., Liu, Q.: Lattice Boltzmann methods for multiphase flow and phase-change heat transfer. Progress in Energy and Combustion Science **52**, 62–105 (2016)
24. Mauch, S.P.: Efficient algorithms for solving static hamilton-jacobi equations. Ph.D. thesis, California Institute of Technology (2003)
25. Nathen, P., Gaudlitz, D., Krause, M.J., Adams, N.A.: On the stability and accuracy of the BGK, MRT and RLB Boltzmann schemes for the simulation of turbulent flows. CiCP **23**(3) (2018)

26. Nicoud, F., Ducros, F.: Subgrid-scale stress modelling based on the square of the velocity gradient tensor. Flow, Turbulence and Combustion **62**, 183–200 (1999)
27. Ploumhans, P., Winckelmans, G., Salmon, J., Leonard, A., Warren, M.: Vortex methods for direct numerical simulation of three-dimensional bluff body flows: Application to the sphere at Re=300, 500, and 1000. Journal of Computational Physics **178**(2), 427–463 (2002)
28. Poon, E.K.W., Iaccarino, G., Ooi, A.S.H., Giacobello, M.: Numerical Studies of high Reynolds Number Flow Past a Stationary and Rotating Sphere p. 7 (2009)
29. Reyes Barraza, J.A., Deiterding, R.: A lattice boltzmann method in generalized curvilinear coordinates. In: VI International Conference on Particle-based Methods - Fundamentals and Applications (2019)
30. Shao, W., Li, J.: Review of Lattice Boltzmann Method Applied to Computational Aeroacoustics. Archives of Acoustics **44**(2), 24 (2019)
31. Smagorinsky, J.: General circulation experiments with the primitive equations, I: The basic experiment. Monthly Weather Review **91**(3), 99–164 (1963)
32. Succi, S.: The Lattice Boltzmann Equation for Fluid Dynamics and Beyond. Numerical Mathematics and Scientific Computation. OUP Oxford, Oxford : New York (2001)
33. Tiwari, A., Vanka, S.P.: A ghost fluid lattice Boltzmann method for complex geometries. Int. J. Numer. Meth. Fluids **69**(2), 481–498 (2012)
34. Wang, J., Chen, L., Kang, Q., Rahman, S.S.: The lattice Boltzmann method for isothermal micro-gaseous flow and its application in shale gas flow: A review. International Journal of Heat and Mass Transfer **95**, 94–108 (2016)
35. Xu, A., Shyy, W., Zhao, T.: Lattice Boltzmann modeling of transport phenomena in fuel cells and flow batteries. Acta Mech. Sin. **33**(3), 555–574 (2017)
36. Zhao-Li, G., Chu-Guang, Z., Bao-Chang, S.: Non-equilibrium extrapolation method for velocity and pressure boundary conditions in the lattice Boltzmann method. Chinese Phys. **11**(4), 366–374 (2002)